Tracers in vascular inflammation: Dunphy and colleagues review the role of radionuclide techniques in identifying vulnerable plaque and preview an article on the pathophysiology of atherosclerosis in this issue of *JNM*. . . . . ***Page 1753***

SPECT/CT in lymphatic mapping: van der Ploeg and colleagues assess the additional anatomic value of CT combined with SPECT in localizing sentinel nodes in patients with inconclusive findings in breast cancer or melanoma. . . ***Page 1756***

Optimal SUV for PET N-staging: Hellwig and colleagues determine a recommended threshold for standardized uptake value measurements in staging mediastinal lymph nodes in lung cancer and compare results from its use with those using visual interpretation. . . . . ***Page 1761***

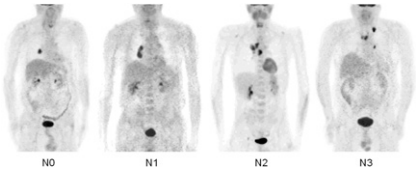

Zevalin and Bexxar compared: Jacene and colleagues report on clinical experience with the respective weight-based and patient-specific dosing regimens of ^{90}Y-ibritumomab tiuxetan and ^{131}I-tositumomab in refractory non-Hodgkin's lymphoma. . . . . ***Page 1767***

β-receptor density and sympathetic function: Tsukamoto and colleagues use ^{11}C-CGP PET to measure myocardial β-adrenergic receptor density in patients with nonischemic cardiomyopathy and compare the results with standard parameters of heart failure, including presynaptic function assessed by ^{123}I-MIBG imaging. . . . . ***Page 1777***

3D cardiac blood flow PET: Schepis and colleagues compare 2D and 3D dynamic ^{13}N-ammonia PET for absolute quantification of myocardial blood flow. ***Page 1783***

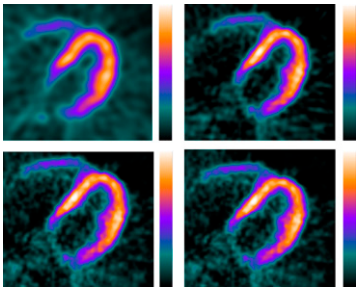

PET/CT in cervical dystonia: Sung and colleagues assess the utility of ^{18}F-FDG PET/CT as an alternative to needle electromyography mapping in identifying affected muscles in patients with idiopathic cervical dystonia before botulinum toxin injection therapy. . . . . ***Page 1790***

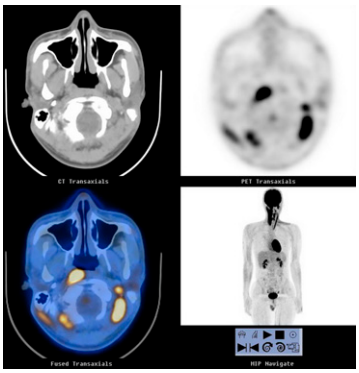

Synthetic SPECT lesion: Abbott and colleagues describe development of and initial studies with a reusable synthetic lesion for in vivo SPECT characterization of lesion detectability, an approach that can serve as a bridge between phantom studies and small animal imaging. . . ***Page 1796***

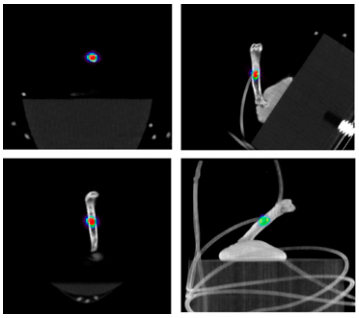

Inflammation and atherosclerosis: Spagnoli and colleagues provide an educational overview of the natural history of atherosclerotic plaques and the molecular pathophysiology of atherosclerosis, with an emphasis on the need for "total patient" perspectives in this chronic inflammatory disorder. . . . . ***Page 1800***

Imaging protein receptors in atheroma: Hartung and colleagues investigate the feasibility of noninvasive radionuclide imaging of inflammation by detection of high concentrations of monocyte chemoattractant protein-1 receptors in inflammatory cells in experimentally induced atherosclerosis. . . . . ***Page 1816***

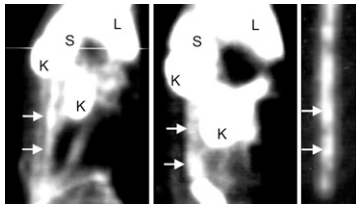

Monitoring minocycline therapy in stroke: Tang and colleagues explore the utility of ^{99m}Tc-annexin V, an in vivo marker of apoptosis, with SPECT to monitor the antiapoptotic effects of minocycline therapy in induced ischemia in a mouse model. . . . . ***Page 1822***

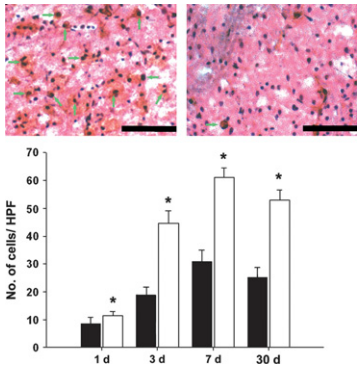

nAChRs after smoking: Mamede and colleagues use ^{123}I-5IA SPECT to explore changes in nicotinic acetylcholine receptors in brains of smokers at 3 time periods

after smoking cessation and identify a "breaking point" in the nicotine withdrawal period. . . . . ***Page 1829***

Liver tissue after RFA: Vogt and colleagues compare MRI, CT, ultrasound, and PET in the assessment of typical lesions after radiofrequency ablation in nontumorous swine liver tissue, to identify an optimal imaging approach for residual tumor. . . ***Page 1836***

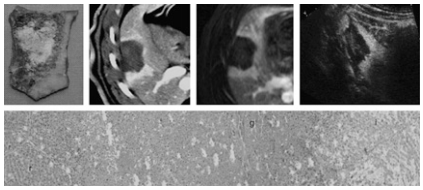

DNA/carrier nanoparticles and streptavidin: Nakamura and colleagues evaluate antisense DNA/streptavidin/carrier nanoparticles for accumulation in cell culture and in xenografted mice to improve cell membrane transport in antisense targeting of tumor cells. . . . . ***Page 1845***

Novel PET ligand for PBR: Zhang and colleagues detail the synthesis and evaluation of a new ^{11}C-labeled PET ligand for imaging peripheral benzodiazepine receptors in the primate and rodent brain. . . . . ***Page 1853***

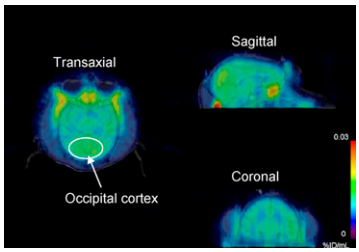

Dual-function PET and optical probe: Cai and colleagues describe the development of a PET/near-infrared fluorescence probe that can facilitate accurate in vivo assessment of the pharmacokinetics and tumor-targeting efficacy of quantum dots. . . . . ***Page 1862***

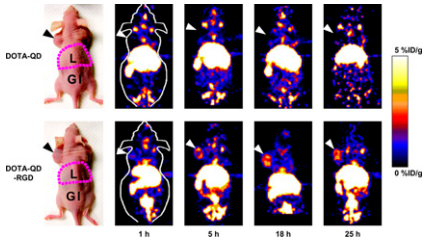

^{90}Y-Ibritumomab tiuxetan dosimetry: Cremonesi and colleagues report on studies designed to identify reliable and feasible dosimetric methods for high-dose ^{90}Y-ibritumomab tiuxetan therapy and autologous stem cell transplantation, as well as safety and optimal timing of stem cell reinfusion. . . . . ***Page 1871***

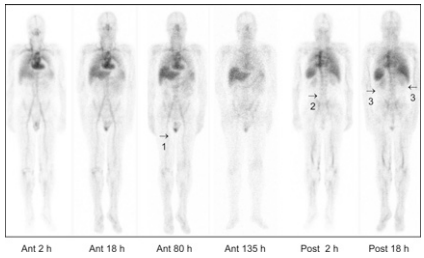

Estimating patient active marrow mass: Pichardo and colleagues describe a simplified CT- or radiography-based method for estimating skeletal spongiosa volume and active marrow mass in the adult male and adult female. . . . . ***Page 1880***

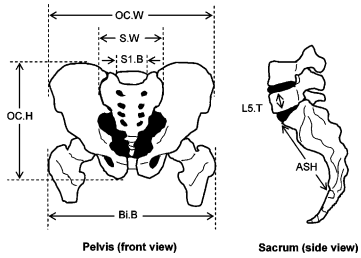

Pulmonary ^{18}F-FDG input function: Schroeder and colleagues present and validate a method to accurately derive an input function from a blood-pool region of interest defined in dynamic PET images for compartmental modeling of ^{18}F-FDG kinetics in the lung. . . . . ***Page 1889***

Radiolabeled egg stability: Knight and colleagues compare the stability of ^{99m}Tc-sulfur colloid–labeled liquid egg white with that of similarly labeled fresh whole eggs and evaluate egg cooking methods for gastric-emptying scintigraphy. ***Page 1897***

NOPR design and analysis: Hillner and colleagues review the data collection and analysis strategies of the National Oncologic PET Registry, which was initiated in response to requirements for collection of clinical and demographic data to extend coverage of PET. . . . . ***Page 1901***

ON THE COVER

In a woman with right breast cancer, planar lymphoscintigraphy (top left) depicts one internal mammary chain sentinel node and a second-echelon node. Axial fused SPECT/CT (top right) and a 3-dimensional SPECT/CT maximum-intensity projection of the thorax (bottom left) enable tracing of the sentinel node, displayed using a color wash, underneath the rib at the second intercostal space close to the right sternal border. In another woman, with left breast cancer (bottom right), axial SPECT/CT shows an interpectoral sentinel node.

See page 1758.